Catalysis Today 165 (2011) 64–70

Contents lists available at ScienceDirect

Catalysis Today

journal homepage: www.elsevier.com/locate/cattod

Understanding of ethanol decomposition on Rh(1 1 1) from density functional theory and kinetic Monte Carlo simulations

YongMan Choi, Ping Liu*

Chemistry Department, Brookhaven National Laboratory, Upton, NY 11973, USA

ARTICLE INFO

Article history:
Received 13 September 2010
Received in revised form 5 December 2010
Accepted 6 December 2010
Available online 12 January 2011

Keywords:
Ethanol decomposition
Rhodium
Alloy
Density functional theory
Kinetic Monte Carlo

ABSTRACT

Reaction mechanisms of ethanol decomposition on Rh(1 1 1) were elucidated by means of periodic density functional theory (DFT) calculations and kinetic Monte Carlo (KMC) simulations. We propose that the most probable reaction pathway is via $CH_3CH_2O^*$ on the basis of our mechanistic study: $CH_3CH_2OH^* \rightarrow CH_3CH_2O^* \rightarrow CH_2CH_2O^* \rightarrow CH_2CHO^* \rightarrow CH_2CO^* \rightarrow CHCO^* \rightarrow CH^* + CO^* \rightarrow C^* + CO^*$. In contrast, the contribution from the pathway via CH_3CHOH^* is relatively small, $CH_3CH_2OH^* \rightarrow CH_3CHOH^* \rightarrow CH_3CHO^* \rightarrow CH_3CO^* \rightarrow CH_2CO^* \rightarrow CHCO^* \rightarrow CH^* + CO^* \rightarrow C^* + CO^*$. According to our calculations, one of the slow steps is the formation of the oxametallacycle $CH_2CH_2O^*$ species, which leads to the production of $CHCO^*$, the precursor for C–C bond breaking. Finally, the decomposition of ethanol leads to the production of C and CO. Our calculations, for ethanol combustion on Rh, the major obstacle is not C–C bond cleavage, but the C contamination on Rh(1 1 1). The strong C–Rh interaction may deactivate the Rh catalyst. The formation of Rh alloys with Pt and Pd weakens the C–Rh interaction, easing the removal of C, and, as expected, in accordance with the experimental findings, facilitating ethanol combustion.

1. Introduction

Ethanol has been considerably attracted in energy applications as a sustainable alternative fuel to gasoline owing to the ease of its transportation and storage, its high lower heating value (LHV) compared to that of gasoline, and its production from biomass [1–4]. In particular, a direct ethanol fuel cell (DEFC) [5] offers distinct potential advantages over internal combustion engines and hydrogen fuel cells for transportation and residential applications. However, the kinetics of the ethanol oxidation reaction is complex and slow, even on the best available catalysts, because several reaction intermediates are generated and the oxidation of ethanol to CO_2 is incomplete, i.e., the C–C bond is not broken except at extreme positive potentials. Alternatively, partial oxidation ($C_2H_5OH + 3/2O_2 \rightarrow 2CO_2 + 3H_2$) and steam reforming ($C_2H_5OH + 3H_2O \rightarrow 2CO_2 + 6H_2$) in an on-board reformer can yield the molecular hydrogen necessary for operating a conventional hydrogen fuel cell. Broadly, improved reforming catalysts for ethanol and other bio-alcohols is important as a source of hydrogen in a hydrogen economy based on renewable fuels. For either of these two processes, a good catalyst must be efficient in C–C bond dissociation, CO or C oxidation, and H–H association. At a molecular or fundamental level, it is not known exactly how the catalysts for the processing of ethanol work. Rh-based catalysts have been applied for both ethanol electrooxidation and steam reforming. Our recent study showed that $RhPt/SnO_2$ is an extremely good catalyst for the electro-oxidation of ethanol, wherein ethanol is converted to CO_2 at low potential and Rh plays an essential role in breaking the C–C bond [2]. In addition, Rh appears to be the most suitable compound in ethanol steam reforming for C–C bond cleavage at reasonable operating temperatures [3]. To date, extended metal surfaces have been considered as model systems to understand the role of metals in the dehydrogenation and oxidation of ethanol, both experimentally [6–14] and computationally [9,14–21]. However, for Rh(1 1 1), the kinetics, mechanisms, and structural information of various intermediate species are not well understood, and such knowledge is crucial to rationally designing better Rh-based catalysts for ethanol combustion.

In this study, we presented the detailed mechanisms for the decomposition reaction of ethanol on Rh(1 1 1) using plane-wave density functional theory (DFT) calculations. On the basis of our DFT results, we used kinetic Monte Carlo (KMC) simulations to generate more practical pictures for designing Rh-based catalysts to gain better understanding of the following: What is the exact role of Rh in the process? How is the C–C bond in ethanol broken? What are the key steps, the intermediates, and the products? How can we improve the catalytic activity of Rh?

* Corresponding author. Tel.: +1 631 344 5970; fax: +1 631 344 5815.
E-mail address: pingliu3@bnl.gov (P. Liu).

0920-5861/$ – see front matter © 2010 Elsevier B.V. All rights reserved.
doi:10.1016/j.cattod.2010.12.017

2. Computational methods

All of DFT calculations were carried out using Cambridge Serial Total Energy Package (CASTEP) in Materials Studio 5.0, similar to our previous studies [22]. We used the generalized gradient approximation of Perdew–Wang (GGA-PW91) [23]. The ionic core is represented by ultrasoft pseudopotentials [24], and a 300 eV cut-off energy was used. All the results discussed in this study come from non-spin polarization calculations with the density mixing scheme [25]. We applied Monkhorst–Pack [26] mesh k-points of $(4 \times 4 \times 1)$ for surface calculations. To examine the effect of the number of Rh layers on surface calculations, we systematically evaluated the adsorption energy of ethanol using three, four, and five atomic-layer p(2×2) surfaces separated by a vacuum space of 15 Å in the direction perpendicular to the surface, resulting in a negligible effect (−0.37 eV using three layers, −0.37 eV using four layers and −0.41 eV using five layers). Only the top-most layer was relaxed. Thus similar to a previous study [27], to reduce computational time, we used three-layer p(2×2) Rh(1 1 1) surfaces. Similarly, we checked the effect of the number of fixed layers on surface calculations using the three layer p(2×2): Relaxing one, two, and three top-most layers engenders only a slight change (−0.37 by allowing one topmost layer to relax, −0.38 eV by allowing two top layers to relax, and −0.41 eV by allowing three top layers to relax). Thus, in this study, only the top-most layer and adsorbates were fully relaxed, while two bottom layers were fixed. For transition state search calculations, the linear and quadratic synchronous transit (LST/QST) method was used [28]. In this study, adsorption energies were calculated according to $\Delta E_{ads} = E$[adsorbate-Rh(1 1 1)] − E[Rh(1 1 1)] − E[adsorbate], where E[adsorbate-Rh(1 1 1)], E[Rh(1 1 1)], and E[adsorbate] are the calculated electronic energies of an adsorbed species on Rh(1 1 1), pure Rh(1 1 1), and an adsorbate. Reaction energies (ΔE), for example, AB → A + B, were estimated by E[A-Rh(1 1 1)] + E[B-Rh(1 1 1)] − E[Rh(1 1 1)] − E[AB-Rh(1 1 1)]. KMC calculations were performed with Kinetix, a newly implemented software in Materials Studio 5.0 [29].

3. Results and discussion

3.1. Mechanisms of ethanol decomposition on Rh(1 1 1) based on DFT calculations

To elucidate the reaction mechanisms of ethanol decomposition on Rh(1 1 1), we first examined molecular ethanol adsorption. In this study, "*" indicates adsorbed surface species, and the most stable configurations of C*, H*, CH*, CH_2*, CH_3*, CO*, and OH* (respectively, hcp, fcc, hcp, hcp, atop, atop, and fcc sites) were applied to estimated reaction energies for elementary steps. We found that ethanol adsorption occurs through the donation of lone pair electrons to surface forming a η^1(O)-configuration and the C–C bond is almost perpendicular to the surface (see Fig. 1). It is consistent with a systematic study by Yang and coworkers, showed that ethanol is adsorbed with the same configuration of the coverage of 1/9 to 1/3 ML [15]. Our calculated adsorption energy of ethanol at 1/4 ML is in good agreement with a published value (−0.33 eV versus −0.36 eV) [15]. In addition to the most stable structure, we also examined the η^1(O)-configuration with the C–C bond of ethanol tilted towards the surface, finding that it is 0.05 eV unstable. We note that the choice of an isomer parallel to the surface changes a reaction barrier (E_a), for example, E_a for the dehydrogenation of the β-position H (CH_3) to CH_2CH_2OH* is lowered from 1.81 eV to 0.78 eV, opening a comparative pathway to the dehydrogenation of ethanol to CH_3CHOH* and CH_3CH_2O*. Therefore, for consistency with the previous studies [15,30], we only applied the most stable structure for the present mechanistic study.

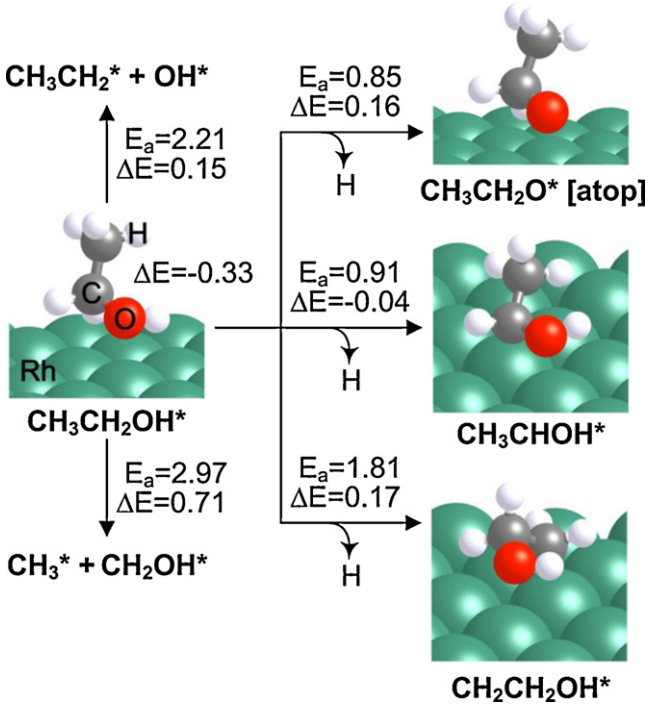

Fig. 1. First dehydrogenation reactions and the cleavage of the C–C and C–O bonds of adsorbed ethanol on Rh(1 1 1). CH_3CH_2O* is the **atop** configuration. Energy is in units of eV. "**atop**" is the CH_3CH_2O* intermediate bound to the atop site of rhodium. Hydrogen, carbon, oxygen, and rhodium are in white, gray, red, and cyan, respectively. (For interpretation of the references to color in this figure legend, the reader is referred to the web version of the article.)

Fig. 1 clearly shows that the C–C and C–O bond breakings of ethanol have higher barriers (E_a: 2.97 and 2.21 eV, respectively) than the dehydrogenation of ethanol. No detailed studies on the first three dehydrogenation on Rh(1 1 1) are available. Previous DFT studies showed that CH_3CHOH* is preferentially produced on Pd(1 1 1) [14,20] and Pt(1 1 1) [18,31]. Experimentally, the first dehydrogenation forming CH_3CH_2O* occurs on Rh(1 1 1) at ∼220 K [7], Pt(1 1 1) at 180 K [13], and Co(0 0 1) at 160 K [9]. We carefully examined the reaction barriers of the three possible steps for the first dehydrogenation of ethanol on Rh(1 1 1). As discussed, C_β-H breaking forming CH_2CH_2OH* must overcome a high barrier of 1.81 eV (Fig. 1). In contrast, the formations of CH_3CH_2O* via O–H cleavage and CH_3CHOH* via C_α–H cleavage are more likely to occur, while the O–H breaking are slightly favored (0.85 eV versus 0.91 eV). It was reported that ethoxy species (CH_3CH_2O) in vacuum are easily formed along with replacing the O–H bond to a Rh–O bond according to careful measurements using high resolution electron energy loss spectroscopy (HREELS) [6]. Thus, in our calculations, we considered both CH_3CH_2O* and CH_3CHOH* species for the sequential reaction. Another crucial point is that the detailed information about the orientation of the ethoxy species on Rh(1 1 1) has not been reported in the literature. Thus as a starting point, we used the results reported Xu et al. on Ni(1 1 1) [12] to examine the most stable structure and active site of CH_3CH_2O*. They analyzed ethoxy species generated on Ni(1 1 1) at 90 K using infrared reflection absorption spectroscopy (IRAS) [12], attributing the peak at 2875 cm^{-1} to the symmetric stretching of CH_2, while 2964 cm^{-1} was assigned to the asymmetric mode for CH_3. These assignments suggest that the C–O bond of ethoxy species is bound perpendicularly to the surface; otherwise, the symmetric stretching mode of CH_2 would not exist. Our vibration-mode analyses for the ethoxy species on Rh(1 1 1) (see Fig. 2) clearly show that only

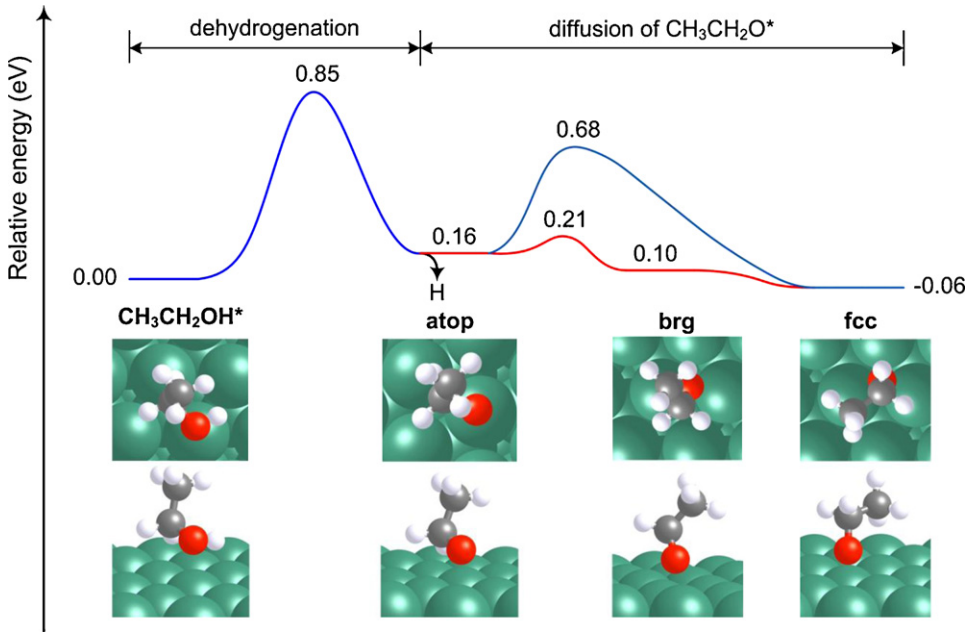

Fig. 2. Schematic of $CH_3CH_2OH^*$ dehydrogenation forming $CH_3CH_2O^*$ and $CH_3CH_2O^*$ diffusion processes on Rh(1 1 1). "**atop**", "**brg**", and "**fcc**" are $CH_3CH_2O^*$ intermediates bound to the atop, bridge, and threefold fcc sites, respectively. Hydrogen, carbon, oxygen, and rhodium are in white, gray, red, and cyan, respectively. (For interpretation of the references to color in this figure legend, the reader is referred to the web version of the article.)

the **fcc** configuration with C–O bond perpendicular to the surface has a symmetric stretching for CH_2 at 2978 cm^{-1}. However, because only that of C_2D_5O on Rh(1 1 1) is available (2110 cm^{-1}) in the literature [6], we predicted the CH_2 stretching of deuterated C_2D_5O at 2158 cm^{-1}, which is in good agreement with the experimental value. Our DFT calculations show that the stability of ethoxy species follows the decreasing sequence **fcc** > **hcp** > **brg** (**bridge**) > **atop**; the relative adsorption energy with respect to the most stable at **fcc** are 0.00, 0.02, 0.16, and 0.22 eV, respectively. As shown in Fig. 2, reaction barriers for the diffusion of $CH_3CH_2O^*$ from **atop** to **fcc** and from **atop** to **brg** are much lower than that of $CH_3CH_2O^*$ formation from ethanol dehydrogenation. In addition, the diffusion from **brg** to **fcc** is almost barrierless. Therefore, it is reasonable to interpret that the ethoxy species generated from decomposition of ethanol at the atop site of Rh(1 1 1) is bound to the atop site first, and then diffused to the three-fold hollow sites via the **brg** site with a barrier as low as 0.05 eV.

As discussed above, we took into account of the pathways via both $CH_3CH_2O^*$ and CH_3CHOH^*. As shown in Fig. 3, along the pathway via $CH_3CH_2O^*$, $CH_2CH_2O^*$ is much more favorably formed from $CH_3CH_2O^*$ dehydrogenation, rather than CH_3CHO^* and $CH_3^* + CH_2O^*$ (E_a: 0.95 eV versus 1.76 eV and 2.98 eV, respectively). Our results follow the mechanism proposed by Houtman and Barteau [6]. Based on their experiments using temperature programmed desorption (TPD) and HREELS techniques, they found that the dehydrogenation of $CH_3CH_2O^*$ to $CH_2CH_2O^*$ is the major route, rather than via CH_3CHO^*. In addition, $CH_2CH_2O^*$ preferentially is dehydrogenated to CH_2CHO^* after overcoming a 0.13 eV barrier, indicating that it is a much faster kinetics compared to the $CHCH_2O^*$ formation with a barrier of 1.42 eV. It means that the reaction runs via $CH_2CH_2O^*$ that has a short life time due to the fast sequential dehydrogenation. This finding is able to well explain the experimental observation, wherein the $CH_2CH_2O^*$ species was proposed only as the intermediates for ethanol on Rh and has never been observed experimentally [3,6,32]. CH_2CHO^* with a flat structure to the surface favors the formation of CH_2CO^* (E_a = 0.43 eV) via C_α–H cleavage rather than $CHCHO^*$ via C_β–H (E_a = 0.65 eV), which is followed by the production of $CHCO^*$ (E_a = 0.83 eV). The C–C bond cleavage of $CHCO^*$ (E_a = 0.69 eV) is energetically preferred over the dehydrogenation to CCO^* (E_a = 0.97 eV). Our calculations show that with a barrier of 0.69 eV, C–C bond breaking is not the major obstacle for ethanol decomposition on Rh, as suggested experimentally [4]. In contrast, more difficult steps, such as ethanol dehydrogenation to $CH_3CH_2O^*$ (E_a = 0.85 eV, Fig. 1) and $CH_2CH_2O^*$ formation from $CH_3CH_2O^*$ dehydrogenation (E_a = 0.95 eV, Fig. 3), are identified in our calculations. The efficient C–C bond cleavage on Rh(1 1 1) is due to the strong interaction between Rh and CHCO (adsorption energy, −3.20 eV), which leads to a stretched C–C bond of CHCO by 0.13 Å compared to that in gas phase and the electron density transfer of 1.17e from Rh to CHCO.

Along the pathway via the CH_3CHOH^* intermediate (Fig. 4), CH_3CHOH^* can be dehydrogenated to CH_2CHOH^* and CH_3COH^* with E_a = 1.68 eV and E_a = 1.24 eV, respectively, but preferentially to CH_3CHO^* after overcoming a much lower barrier (E_a = 0.72 eV). Then CH_3CHO^* is quickly transformed to CH_3CO^* rather than to CH_2CHO^* (E_a = 0.23 eV versus 0.55 eV, respectively). Further dehydrogenation of CH_3CO^* produces CH_2CO^* with an apparently high barrier of 1.47 eV, and then the rest of reactions follows that of CH_2CO^* in the pathway via CH_3CHOH^*.

Overall, our DFT calculations suggest two possible reaction pathways for ethanol decomposition, that is, via $CH_3CH_2O^*$ or CH_3CHOH^*, which may run in parallel during its ethanol decomposition on Rh(1 1 1). Both pathways lead to the formation of $CHCO^*$, which seems to be the important precursor for the C-C bond breaking on Rh(1 1 1) and eventually produces C^* and CO^* from ethanol. This will be discussed in more detail with the KMC modeling below.

3.2. KMC simulations of ethanol decomposition on Rh(1 1 1)

In order to propose the most probable pathway for ethanol decomposition on Rh(1 1 1), we carried out KMC simulations, keeping our model as simple as possible. It is known that reaction barriers and adsorption energies are coverage-dependent [12,15]. In this study, accurate examination of desorption barriers is beyond the scope of our study. Thus, we excluded the desorption process and considered those processes summarized in Table 1, where the

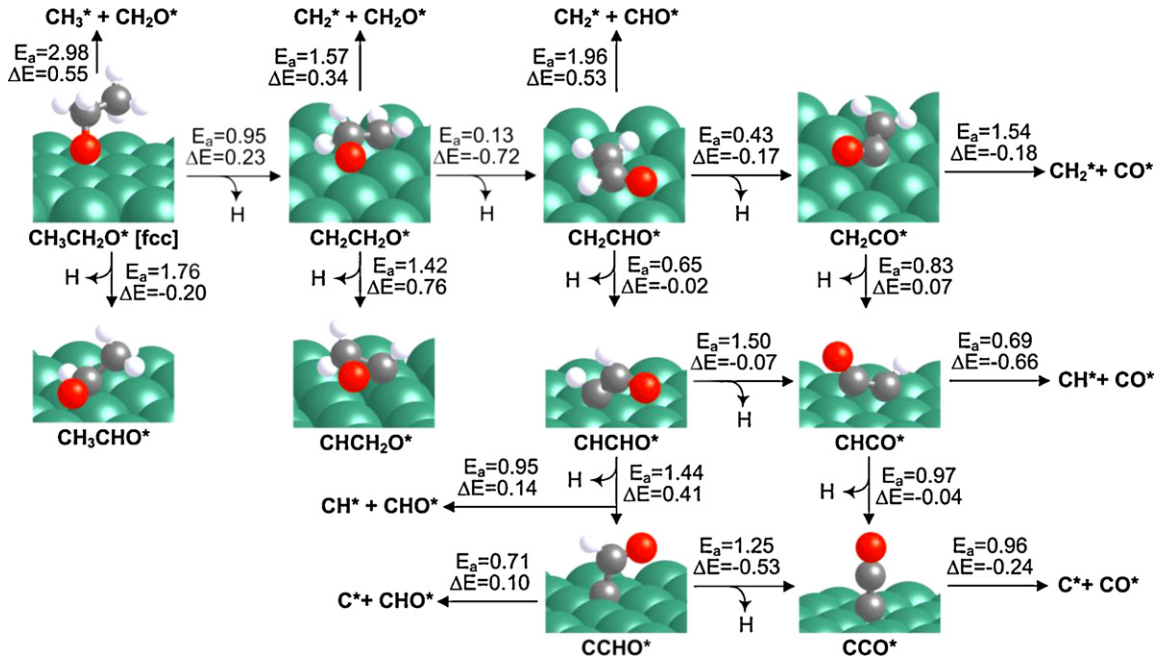

Fig. 3. Reaction sequences for the dehydrogenation and scission of C–C bonds from the $CH_3CH_2O^*$ intermediate. Energy is in units of eV. Hydrogen, carbon, oxygen, and rhodium are in white, gray, red, and cyan, respectively. (For interpretation of the references to color in this figure legend, the reader is referred to the web version of the article.)

pathways via both CH_3CHOH^* and $CH_3CH_2O^*$ are included. In addition, because Papageorgopoulou et al. [7] experimentally confirmed that there was no contribution from the recombination reaction of $CH_3CH_2O^*$ and dissociated hydrogen species forming ethanol, we only considered forward reactions in the KMC simulations. We used the identical prefactors of $1.0 \times 10^{13}\ s^{-1}$ as in previous studies [33]. We carried out KMC calculations at $\theta = 0.1$ monolayer (ML), which is close to an experimental value (0.13 ML) [6]. Adsorption was performed at 100 K and then, up to 800 K with a heating rate of $4.0\ K\ s^{-1}$. In addition, we assumed the $CH_3CH_2O^*$ formation is one-step process ($CH_3CH_2OH^* \rightarrow CH_3CH_2O^*$ [**fcc**] + H^*, $E_a = 0.85$ eV), as discussed above.

According to our KMC simulations, as temperatures increase, the coverage of ethanol on Rh(1 1 1) decreases to zero, while carbon and carbon monoxide are eventually produced along with associative H_2 desorption (Fig. 5a). In terms of intermediates, a significant amount of $CH_3CH_2O^*$, CH_3CO^*, and CH^* were observed (Fig. 5b); in contrast, the coverage of the other intermediates included in Table 1 are much less and cannot compete. According to our DFT calculations (Figs. 3 and 4), CH_3CO^* is produced from

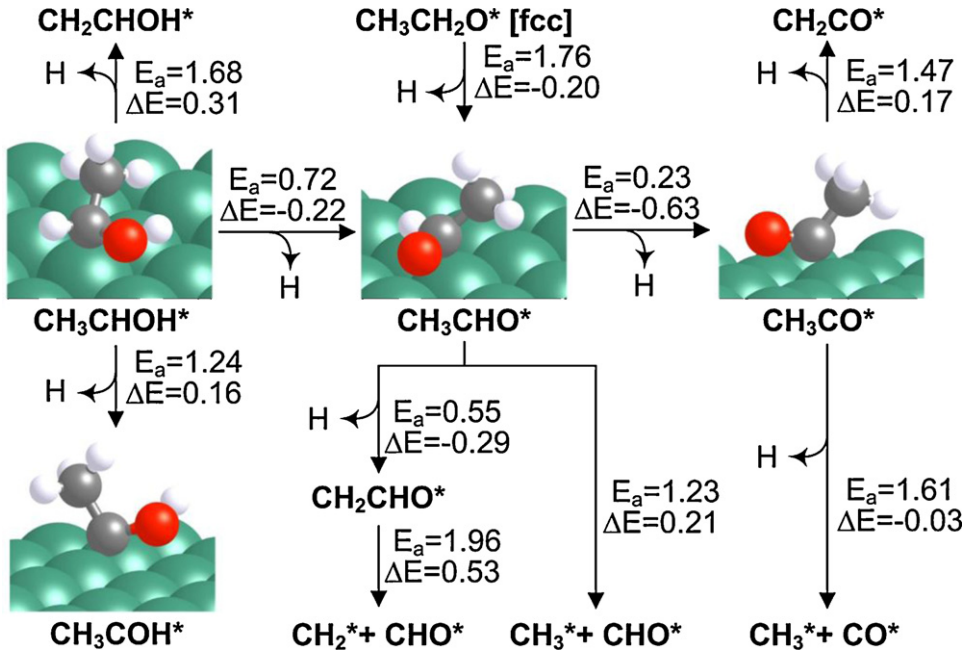

Fig. 4. Reaction sequences for dehydrogenation and scission of C–C bonds from the CH_3CHOH^* intermediate. Energy is in units of eV. Hydrogen, carbon, oxygen, and rhodium are in white, gray, red, and cyan, respectively. (For interpretation of the references to color in this figure legend, the reader is referred to the web version of the article.)

Table 1
Summary of reaction barriers[a] and reaction energies in eV for elementary steps of ethanol decomposition on Rh(1 1 1).

Elementary reaction	E_a (eV)	ΔE (eV)
$CH_3CH_2OH(g) + * \rightarrow CH_3CH_2OH^*$		−0.33
$CH_3CH_2OH^* + * \rightarrow CH_3CH_2O^*$ [**atop**] $+ H^*$	0.85	0.16
$CH_3CH_2OH^* + * \rightarrow CH_2CH_2OH^* + H^*$	1.81	0.17
$CH_3CH_2OH^* + * \rightarrow CH_3CHOH^* + H^*$	0.91	−0.04
$CH_3CH_2O^*$ [**fcc**] $+ * \rightarrow CH_2CH_2O^* + H^*$	0.95	0.23
$CH_3CH_2O^*$ [**fcc**] $+ * \rightarrow CH_3CHO^* + H^*$	1.76	−0.20
$CH_3CHOH^* + * \rightarrow CH_3CHO^* + H^*$	0.72	−0.22
$CH_3CHOH^* + * \rightarrow CH_2CHOH^* + H^*$	1.68	0.31
$CH_3CHOH^* + * \rightarrow CH_3COH^* + H^*$	1.24	0.16
$CH_2CH_2O^* + * \rightarrow CH_2CHO^* + H^*$	0.13	−0.72
$CH_2CH_2O^* + * \rightarrow CHCH_2O^* + H^*$	1.42	0.76
$CH_2CHO^* + * \rightarrow CHCHO^* + H^*$	0.65	−0.02
$CHCHO^* + * \rightarrow CHCO^* + H^*$	1.50	−0.08
$CHCHO^* + * \rightarrow CCHO^* + H^*$	1.44	0.41
$CCHO^* + * \rightarrow CCO^* + H^*$	1.25	−0.53
$CH_3CHO^* + * \rightarrow CH_3CO^* + H^*$	0.23	−0.63
$CH_3CHO^* + * \rightarrow CH_2CHO^* + H^*$	0.55	−0.29
$CH_2CHO^* + * \rightarrow CH_2CO^* + H^*$	0.43	−0.17
$CH_3CO^* + * \rightarrow CH_2CO^* + H^*$	1.47	0.17
$CH_2CO^* + * \rightarrow CHCO^* + H^*$	0.83	0.07
$CHCO^* + * \rightarrow CCO^* + H^*$	0.97	−0.04
$CH_3^* + * \rightarrow CH_2^* + H^*$	0.72	−0.02
$CH_2^* + * \rightarrow CH^* + H^*$	0.12	−0.41
$CH^* + * \rightarrow C^* + H^*$	1.16	0.38
$CHO^* + * \rightarrow CO^* + H^*$	0.23	−0.88
$CH_3CH_2OH^* + * \rightarrow CH_3^* + CH_2OH^*$	2.97	0.71
$CH_3CH_2O^*$ [**fcc**] $+ * \rightarrow CH_3^* + CH_2O^*$	2.98	0.55
$CH_2CH_2O^* + * \rightarrow CH_2^* + CH_2O^*$	1.57	0.34
$CH_3CHO^* + * \rightarrow CH_3^* + CHO^*$	1.23	0.21
$CH_2CHO^* + * \rightarrow CH_2^* + CHO^*$	1.96	0.53
$CHCHO^* + * \rightarrow CH^* + CHO^*$	0.95	0.14
$CH_3CO^* + * \rightarrow CH_3^* + CO^*$	1.61	−0.03
$CH_2CO^* + * \rightarrow CH_2^* + CO^*$	1.54	−0.18
$CHCO^* + * \rightarrow CH^* + CO^*$	0.69	−0.66
$CCHO^* + * \rightarrow C^* + CHO^*$	0.71	0.10
$CCO^* + * \rightarrow C^* + CO^*$	0.96	−0.24
$CH_3CH_2OH^* + * \rightarrow CH_3CH_2^* + OH^*$	2.21	0.15
$CH_3CHO^* \rightarrow CH_3CHO(g) + *$	0.61	0.61
$H^* + H^* \rightarrow H_2(g) + 2^*$	0.50	0.50
$CO^* \rightarrow CO(g) + *$	1.82	1.82

[a] "**atop**", "**brg**", and "**fcc**" are CH_3CH_2O intermediates bound to the atop, bridge, and threefold fcc sites, respectively. The reaction barrier and energetics for $CH_3CH_2OH^* + * \rightarrow CH_3CH_2O^*$ [**fcc**] $+ H^*$ are summarized in Fig. 2 (0.85 eV and −0.06 eV, respectively).

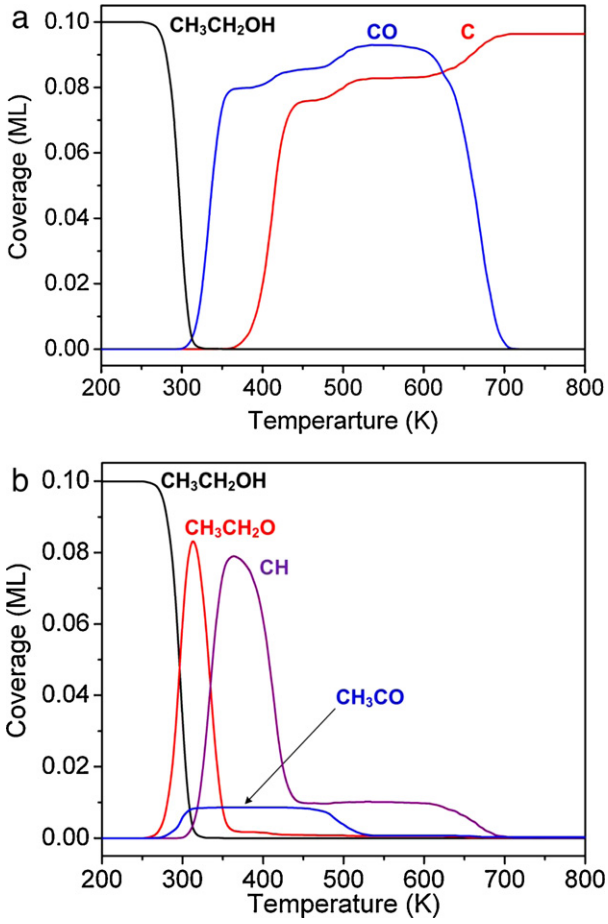

Fig. 5. Temperature-dependent profiles for (a) the reactant of ethanol and products of C and CO and (b) a comparison of ethanol and significant intermediates of $CH_3CH_2O^*$, CH^* and CH_3CO^* simulated using KMC at 0.1 ML of ethanol and the heating rate of 4.0 K s^{-1}.

CH_3CHOH^* via CH_3CHO^* along the CH_3CHOH^* pathway, $CH_3CH_2O^*$ comes from the $CH_3CH_2O^*$ pathway, and CH^* can be the product of $CHCO^*$ produced from both pathways. That is, the KMC results confirm the predictions of the two parallel pathways calculated by the DFT calculations, detailed in Section 3.1, as summarized in Fig. 6. From Fig. 5, we see that the coverage of CH_3CO^* is lower than that of $CH_3CH_2O^*$. In addition, the production of CO^* and CH^* or C^* mostly follow the variations in the coverage of $CH_3CH_2O^*$. The contribution from CH_3CO^* is relatively small, and can only be observed at high temperatures. It is associated with the slightly higher barrier for producing CH_3CHOH^* from ethanol than that of $CH_3CH_2O^*$, which indeed results in the smaller amount of CH_3CO^* produced by the facile dehydrogenation of CH_3CHOH^* (Fig. 6) than that of $CH_3CH_2O^*$. On the other hand, the high activation barrier for the dehydrogenation of CH_3CO^* to CH_2CO^* hinders the production of $CHCO^*$, and therefore, CO^*, CH^* and C^* (Fig. 6). Given that, the pathway via $CH_3CH_2O^*$ is more significant than that via CH_3CHOH^* for ethanol decomposition on Rh(1 1 1) then: $CH_3CH_2OH^* \rightarrow CH_3CH_2O^* \rightarrow CH_2CH_2O^* \rightarrow CH_2CHO^* \rightarrow CH_2CO^* \rightarrow CHCO^* \rightarrow CH^* + CO^* \rightarrow C^* + CO^*$; for clarity, the hydrogen species were omitted.

As mentioned above, the present KMC simulations are simplified to give a qualitative description of the kinetics, e.g., the key intermediates and products. Hence, we cannot quantitatively compare the findings from our simulations with the experiment results. First, our predictions of C and CO as the final products for ethanol decomposition on Rh(1 1 1) agree well with the experiments [6,7]. However, the complete desorption of CO from Rh(1 1 1) was ~550 K from a TPD experiment [6], which is lower than 700 K shown in Fig. 5. In addition, this figure shows that $CH_3CH_2O^*$ is produced at ~260 K, which is slightly off from the experimental finding (~220 K at 1.5 K s^{-1}) reported by Papageorgopoulos et al. [7]. Many factors contribute to the differences. One is that the present DFT calculations with GGA-PW91 overestimate the binding energy [34]. Besides, the DFT may not reproduce the reaction barrier measured experimentally [35]. Finally, it is expected that consideration of lateral interactions affects the rates of each elementary step [36,37]. In this study, we showed that our KMC calculations with well-established mechanisms give a good qualitative description of the experimentally detected intermediate species and products. Again, more detailed mechanistic studies as a function of coverage based on more accurate theory may offer a better picture.

3.3. Understanding the promoting effect of Rh alloys

According to our simulations and the precious experiments [6,7], it is clear that the surface carbon species are one of major products from ethanol decomposition on Rh(1 1 1), which are difficult to be removed due to the strong C–Rh interaction and therefore may deactivate the Rh catalyst during ethanol combustion. Given that, to make Rh more efficient, one of the possible

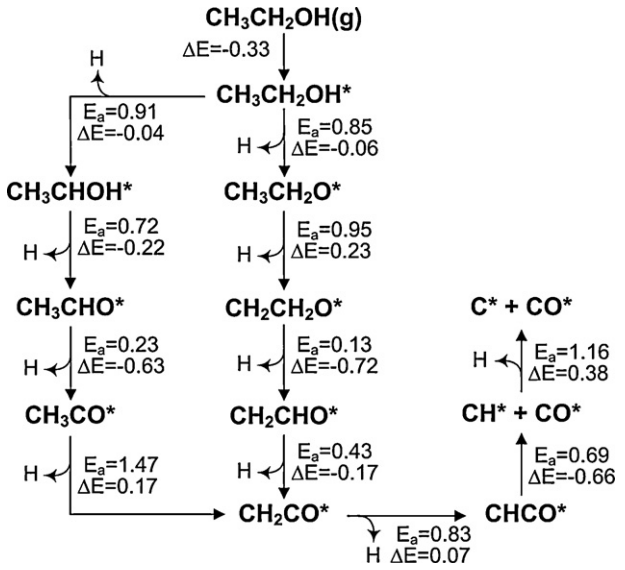

Fig. 6. Proposed reaction pathways for ethanol decomposition on Rh(1 1 1). Energy is in units of eV.

ways is to weaken the C–Rh interaction by introducing promoters, which help the C removal in the form of CO_2. Improved activities have been reported for the Rh alloys with Pt and Pd for ethanol combustion [3,38–41]. Here, we compared the Gibbs free energy changes (ΔG) of removing C from these Rh alloys via reaction, $C^* + 2H_2O(l) \leftrightarrow CO_2(g) + 2H_2(g)$. To describe the Rh alloys, a simplified model was built, where one of Rh atoms on the top-most layer was replaced with an alloying metal. The calculated adsorption energies at 0 K for pure Rh and Rh alloyed with Pt and Pd are −7.79, −6.85, and −6.97 eV, respectively, where the carbon atom adsorbs at the hcp sites of Rh. Consequently, the estimated ΔG ($\Delta G \approx \Delta E_{ads} - T\Delta S$) corresponds to 9.57 eV on Rh, 8.63 eV on RhPt, and 8.75 eV on RhPd, where the Gibbs free energies for $H_2O(l)$ and $CO_2(g)$ are from the literature (−2.45 and −4.09 eV, respectively) [42]. That is, the presence of Pt or Pd weakens the C–Rh interaction and makes the C removal or C oxidation easier, which releases the C-contamination on Rh. In this way, the more efficient production of H_2 can be achieved from ethanol combustion on RhPt and RhPd alloys, which is consistent with the experimental observations [3,38–41].

In general, ethanol combustion includes two steps: one involves dehydrogenation and C–C bond breaking; the other involves CO and C removal in the form of CO_2. In agreement with previous experiments, the first step proceeds well on Rh as demonstrated above. The problem is the slow second step due to the strong C–Rh interaction. One of the possible ways to facilitate the removal of C is to introduce promoters, such as Pd and Pt, which weaken the C–surface interaction.

4. Conclusions

The combined DFT study and KMC simulations were employed to gain a better understanding of the kinetics for ethanol decomposition on Rh(1 1 1). Our results show that ethanol on Rh(1 1 1) is decomposed into C and CO, consistent with the previous experimental findings [6,7]. Two pathways via CH_3CHOH^* or $CH_3CH_2O^*$ may run in parallel. However, the reaction via the $CH_3CH_2O^*$ pathway contributes more. That is, the most probable reaction pathway is: $CH_3CH_2OH^* \rightarrow CH_3CH_2O^* \rightarrow CH_2CH_2O^* \rightarrow CH_2CHO^* \rightarrow CH_2CO^* \rightarrow CHCO^* \rightarrow CH^* + CO^* \rightarrow C^* + CO^*$. A surface oxametallacycle CH_2CH_2O is an important intermediate rather than CH_3CHO^*, which leads to the formation of $CHCO^*$, the precursor for C–C bond breaking. According to our calculations, for ethanol combustion on Rh, the major obstacle is not C–C bond cleavage, but the C contamination on Rh(1 1 1). The surface carbon species produced from ethanol decomposition are difficult to remove due to the strong C–Rh interaction, which may deactivate the Rh catalyst during ethanol combustion. We found that alloying Rh with Pt or Pd weakens the C interaction and may facilitate the removal of C in the form of CO_2. Therefore, in accordance with the experiments, faster ethanol combustion is expected. This systematic molecular level study clearly guides the understanding of surface reactions including kinetics and the proposing of novel better catalysts for ethanol combustion.

Acknowledgements

This research was carried out at Brookhaven National Laboratory under Contract DE-AC02-98CH10886 with the U.S. Department of Energy (Division of Chemical Sciences). Y.C. thanks Drs. Laura Barrio-Pliego, Joon Bum Park, Sanjaya Senanayake, Dario Stacchiola, and Fan Yang for fruitful discussions of characterization methods for surface reactions, Drs. Altaf Karim and Victor Milman for kind instructions related to KMC simulations, and Dr. Weiping Zhou for continuous discussions of electro-oxidation of ethanol on electrocatalysts. Also, Y.C. also appreciates Prof. Jeng-Han Wang for fruitful discussions about ethanol decomposition on Rh(1 1 1). We acknowledge valuable experimental information from Prof. Hicham Idriss. DFT calculations were performed at the Center for Functional Nanomaterials at Brookhaven National Laboratory and the National Energy Research Scientific Computing (NERSC) Center. Y.C. is pleased to acknowledge Prof. M.C. Lin for CPU time and helpful discussions on ethanol utilization in high temperature fuel cells.

References

[1] A. Kowal, M. Li, M. Shao, K. Sasaki, M.B. Vukmirovic, J. Zhang, N.S. Marinkovic, P. Liu, A.I. Frenkel, R.R. Adzic, Nature Mater. 8 (2009) 325–330.
[2] M. Li, A. Kowal, K. Sasaki, N. Marinkovic, D. Su, E. Korach, P. Liu, R.R. Adzic, Electrochim. Acta 55 (2010) 4331–4338.
[3] H. Idriss, Platinum Met. Rev. 48 (2004) 105–115.
[4] H. Idriss, M. Scott, J. Llorca, S.C. Chan, W. Chiu, P.-Y. Sheng, A. Yee, M.A. Blackford, S.J. Pas, A.J. Hill, F.M. Alamgir, R. Rettew, C. Petersburg, S.D. Senanayake, M.A. Barteau, ChemSusChem 1 (2008) 905–910.
[5] F. Vigier, S. Rousseau, C. Coutanceau, J.-M. Leger, C. Lamy, Top. Catal. 40 (2006) 111–121.
[6] C.J. Houtman, M.A. Barteau, J. Catal. 130 (1991) 528–546.
[7] D.C. Papageorgopoulos, Q. Ge, D.A. King, J. Phys. Chem. 99 (1995) 17645–17649.
[8] E. Vesselli, A. Baraldi, G. Comelli, S. Lizzit, R. Rosei, ChemPhysChem 5 (2004) 1133–1140.
[9] C.J. Weststrate, H.J. Gericke, M.W.G.M. Verhoeven, I.M. Ciobc, A.M. Saib, J.W. Niemantsverdriet, J. Phys. Chem. Lett. 1 (2010) 1767–1770.
[10] B.A. Sexton, Surf. Sci. 88 (1979) 299–318.
[11] B.A. Sexton, K.D. Rendulic, A.E. Huges, Surf. Sci. 121 (1982) 181–198.
[12] J. Xu, X. Zhang, R. Zenobi, J. Yoshinobu, Z. Xu, J.T. Yates Jr., Surf. Sci. 256 (1991) 288–300.
[13] A.F. Lee, D.E. Gawthrope, N.J. Hart, K. Wilson, Surf. Sci. 548 (2004) 200–208.
[14] G. Cui, S. Song, P.K. Shen, A. Kowal, C. Bianchini, J. Phys. Chem. C 113 (2009) 15639–15642.
[15] M.-M. Yang, X.-H. Bao, W.-Z. Li, J. Phys. Chem. C 111 (2007) 7403–7410.
[16] J.-H. Wang, C.S. Lee, M.C. Lin, J. Phys. Chem. C 113 (2009) 6681–6688.
[17] P. Ferrin, D. Simonetti, S. Kandoi, E. Kunkes, J.A. Dumesic, J.K. Nørskov, M. Mavrikakis, J. Am. Chem. Soc. 131 (2009) 5809–5815.
[18] H.-F. Wang, Z.-P. Liu, J. Phys. Chem. C 111 (2007) 12157–12160.
[19] H.-F. Wang, Z.-P. Liu, J. Am. Chem. Soc. 130 (2008) 10996–11004.
[20] M. Li, W. Guo, R. Jiang, L. Zhao, H. Shan, Langmuir 26 (2009) 1879–1888.
[21] E.D. Wang, J.B. Xu, T.S. Zhao, J. Phys. Chem. C 114 (2010) 10489–10497.
[22] P. Liu, J.A. Rodriguez, J.T. Muckerman, J. Hrbek, Phys. Rev. B 67 (2003) 155416.
[23] J.P. Perdew, Y. Wang, Phys. Rev. B 45 (1992) 13244–13249.
[24] D. Vanderbilt, Phys. Rev. B 41 (1990) 7892–7895.
[25] G. Kresse, J. Furthmüller, Phys. Rev. B 54 (1996) 11169–11186.
[26] H.J. Monkhorst, J.D. Pack, Phys. Rev. B 13 (1976) 5188–5192.
[27] Y. Choi, P. Liu, J. Am. Chem. Soc. 131 (2009) 13054–13061.
[28] N. Govind, M. Petersen, G. Fitzgerald, D. King-Smith, J. Andzelm, Comput. Mater. Sci. 28 (2003) 250–258.

[29] J.J. Lukkien, J.P.L. Segers, P.A.J. Hilbers, R.J. Gelten, A.P.J. Jansen, Phys. Rev. E 58 (1998) 2598–2610.
[30] N. Kapur, J. Hyun, B. Shan, J.B. Nicholas, K. Cho, J. Phys. Chem. C 114 (2010) 10171–10182.
[31] R. Alcala, M. Mavrikakis, J.A. Dumesic, J. Catal. 218 (2003) 178–190.
[32] N.F. Brown, M.A. Barteau, Surf. Sci. 298 (1993) 6–17.
[33] P. Liu, J.A. Rodriguez, J. Phys. Chem. B 110 (2006) 19418–19425.
[34] B. Hammer, L.B. Hansen, J.K. Nørskov, Phys. Rev. B 59 (1999) 7413–7421.
[35] N. Hansen, T. Kerber, J. Sauer, A.T. Bell, F.J. Keil, J. Am. Chem. Soc. 132 (2010) 11525–11538.
[36] D. Mei, M. Neurock, C.M. Smith, J. Catal. 268 (2009) 181–195.
[37] A.P.J. Jansen, Phys. Rev. B 69 (2004) 035414.
[38] P.Y. Sheng, A. Yee, G.A. Bowmaker, H. Idriss, J. Catal. 208 (2002) 393–403.
[39] P.Y. Sheng, H. Idriss, J. Vac. Sci. Technol. A 22 (2004) 1652–1658.
[40] M. Scott, M. Goeffroy, W. Chiu, M. Blackford, H. Idriss, Top. Catal. 51 (2008) 13–21.
[41] J.P.I. de Souza, S.L. Queiroz, K. Bergamaski, E.R. Gonzalez, F.C. Nart, J. Phys. Chem. B 106 (2002).
[42] NIST-JANAF Thermochemical Tables (Journal of Physical and Chemical Reference Data Monographs), Springer-Verlag New York, LLC, 1998.